

Structural changes in Li_2MnO_3 cathode material for Li-ion batteries

Jatinkumar Rana,^{*,†} Marian Stan,[‡] Richard Kloepsch,[‡] Jie Li,[‡] Gerhard Schumacher,[†] Edmund Welter,[¶] Ivo Zizak,[†] John Banhart,^{†,§} and Martin Winter[‡]

Helmholtz-Zentrum Berlin für Materialien und Energie, Hahn-Meitner-Platz 1, 14109 Berlin, Germany, Institute of Physical Chemistry, MEET Battery Research Centre, University of Muenster, Corrensstrasse 46, 48149 Muenster, Germany, Deutsches Elektronen-Synchrotron, Notkestrasse 85, 22607 Hamburg, Germany, and Technische Universität Berlin, Hardenbergstrasse 36, 10623 Berlin, Germany

E-mail: jatinkumar.rana@helmholtz-berlin.de

Phone: +49 (030)8062 42816. Fax: +49 (030)8062 43059

Abstract

Structural changes in Li_2MnO_3 cathode material for rechargeable Li-ion batteries were investigated during the 1st and 33rd cycles by X-ray absorption spectroscopy. It is found that both the participation of oxygen anions in redox processes and $\text{Li}^+\text{-H}^+$ exchange play an important role in the electrochemistry of Li_2MnO_3 . During activation, oxygen removal from the material along with Li gives rise to the formation of a layered MnO_2 -type structure, while the presence of protons in the interslab region, as a result of electrolyte oxidation and $\text{Li}^+\text{-H}^+$

*To whom correspondence should be addressed

[†]Helmholtz-Zentrum Berlin für Materialien und Energie, Hahn-Meitner-Platz 1, 14109 Berlin, Germany

[‡]Institute of Physical Chemistry, MEET Battery Research Centre, University of Muenster, Corrensstrasse 46, 48149 Muenster, Germany

[¶]Deutsches Elektronen-Synchrotron, Notkestrasse 85, 22607 Hamburg, Germany

[§]Technische Universität Berlin, Hardenbergstrasse 36, 10623 Berlin, Germany

exchange, alters the stacking sequence of oxygen layers from O3-type (ABCABC) to P3-type (ABBCCA). On the other hand, Li re-insertion by exchanging already present protons reverts the stacking sequence of oxygen layers from P3-type back to the original O3-type. The re-lithiated structure closely resembles the parent Li_2MnO_3 , except that it contains less Li and O. Mn^{4+} remains electrochemically inactive at all times. Irreversible oxygen release occurs only during activation of the material in the 1st cycle. During subsequent cycles, electrochemical processes seem to involve unusual redox processes of oxygen anions along with the repetitive, irreversible oxidation of electrolyte species. Li^+ - H^+ exchange during each subsequent cycle involves a repetitive change in the oxygen stacking sequence between O3-type and P3-type. The deteriorating electrochemical performance of Li_2MnO_3 upon cycling is due to the structural degradation caused by repetitive shearing of oxygen layers.

Introduction

The exploration of electrochemical activation in Li_2MnO_3 is important for two main reasons. First, to enhance the fundamental understanding concerning the electrochemistry of Mn^{4+} -containing cathode materials. Second, to obtain the knowledge necessary for designing a possible class of “*Li-rich*” cathodes,¹⁻⁹ where Li_2MnO_3 is an important constituting component. Li_2MnO_3 has an O3 structure where close-packed oxygen layers are stacked in an ABCABC sequence. In a layer notation, Li_2MnO_3 can be written as $\text{Li}[\text{Li}_{1/3}\text{Mn}_{2/3}]\text{O}_2$ where the interslab octahedral sites are occupied by Li only, while the octahedral sites within the $[\text{Li}_{1/3}\text{Mn}_{2/3}]\text{O}_2$ slabs are occupied by both Li and Mn in a ratio of 1 : 2.¹⁰ The fact that in Li_2MnO_3 Mn^{4+} is octahedrally coordinated by O^{2-} led to the initial belief that the material is electrochemically inactive.¹¹ However, this belief was disproved when a substantial charge could be extracted from the material during an activation process that occurs at 4.5 V vs. Li/Li^+ .¹²

Over the past few years, several mechanisms concerning electrochemical activation of Li_2MnO_3 during the 1st charge have been postulated. It has been proposed that Li extraction from Li_2MnO_3 occurs with the simultaneous release of oxygen.¹¹ Later, it was observed that Li extraction occurs

via two competitive processes, namely oxygen removal and $\text{Li}^+ - \text{H}^+$ exchange.¹³⁻¹⁵ The presence of structural defects such as oxygen vacancies also plays an important role in the electrochemical performance of Li_2MnO_3 .^{16,17} While most of these reports elucidate the structural changes upon Li extraction,^{13-15,18} none describes with support by direct experimental evidence from electrochemically treated samples what the structural modifications during Li re-insertion and upon prolonged cycling are.

We study structural modifications in Li_2MnO_3 cathode material during the 1st and 33rd cycles by X-ray absorption spectroscopy (XAS). The elemental selectivity of XAS provides a unique opportunity to probe chemical, electronic and structural changes at and around an absorbing atom. The near-edge region of the absorption spectra is called the X-ray Absorption Near Edge Structure (XANES) and provides qualitative information about the average valence state of absorbing atoms, their local symmetry and electronic configuration. On the other hand, the extended region of the absorption spectra is called the Extended X-ray Absorption Fine Structure (EXAFS) and provides quantitative information about geometrical changes in the vicinity of absorbing atoms. In the present study, the average valence state of Mn and its local symmetry in various Li_2MnO_3 samples are qualitatively discussed in comparison with various manganese reference compounds, while structural changes such as the number of nearest neighbors, interatomic distances and structural disorder are quantified by fitting a theoretical model to the EXAFS data.

Experimental

Li_2MnO_3 was synthesized by a modified Pechini method from acetate precursors.¹⁹ The precursor powders, $\text{Mn}(\text{OCOCH}_3)_2 \cdot 4\text{H}_2\text{O}$ and $\text{Li}(\text{OCOCH}_3) \cdot \text{H}_2\text{O}$ were dissolved in an aqueous mixture of ethylene glycol and citric acid (molar ratio 4 : 1). The mole ratio of ethylene glycol and Mn^{2+} was 10 : 1. Dissolution of reagents was completed by heating to 90 °C with constant stirring followed by a temperature increase to 140 °C to promote esterification. Subsequently, the temperature was increased to 180 °C and maintained for 12 h there, during which the polyester formed. Then, the

temperature was increased to 250 °C and held for 6 h during which the ethylene glycol dried out and the material caramelized. Calcination at 450 °C for 5 h decomposed the precursors and formed Li_2MnO_3 . The calcined Li_2MnO_3 powder was pressed into pellets and annealed at 600 °C for 12 h. The annealed material was characterized for phase purity by X-ray diffraction.

The cathodes for electrochemical characterization were prepared by mixing 80 wt.% active material, 10 wt.% carbon black and 10 wt.% of a solution of polyvinylidene di-fluoride in N-methyl-2-pyrrolidone acting as a binder. The mixture was applied to an aluminum current collector. Electrochemical measurements were carried out in three-electrode Swagelok cells using metallic lithium as a counter and reference electrode. A mixture of ethylene carbonate (EC) and dimethyl carbonate (DMC) (1 : 1 V/V) containing 1 M LiPF_6 was used as electrolyte and a glass fiber filter (Whatman GF/D) as separator. The cells were cycled between 2 V and 5 V vs. Li/Li^+ with a constant current density of 4.6 mA/g (i.e. C/50 with $1\text{C} = 230 \text{ mA/g}$) during the 1st charge and of 23 mA/g (i.e. C/10) during the subsequent cycles using a Maccor Series 4000 battery testing unit. The cells were opened in a dry room and cathodes were washed with DMC solution. The active material was scraped off the aluminum current collector and ground using mortar and pestle. The finely ground powder was uniformly applied to the adhesive-coated Kapton tape using a brush. The powder-coated Kapton tape was cut into several pieces which were stacked on top of each other to form a thin, uniform transmission XAS sample.

XAS measurements were carried out in the transmission mode at the Mn K-edge of various Li_2MnO_3 samples. The samples charged and discharged during the 1st cycle were measured at beamline A1 of the Hamburger Synchrotron Radiation Laboratory (HASYLAB), Hamburg, Germany, while those made during the 33rd cycle were measured at beamline KMC-2 of the BESSY-II synchrotron light source, Berlin, Germany. The former is equipped with a Si (111) double crystal monochromator, while the latter has a graded Si-Ge (111) double crystal monochromator. Higher harmonics were rejected by detuning the monochromator such that the intensity of the beam on the sample was 65 % of the maximum possible intensity. Absolute energy calibration of the monochromator was carried out by measuring a reference foil of pure manganese simultaneously with the

sample. The intensities of the incident beam and beams transmitted through the sample and the reference foil were measured using gas-filled ionization chambers. Besides Li_2MnO_3 samples of interest, various manganese reference compounds such as MnO , Mn_2O_3 , LiMn_2O_4 , MnO_2 -Pyrolusite and KMnO_4 were also measured. All spectra were energy-calibrated with respect to the first peak in the derivative spectrum of pure manganese.

Various data pre-processing operations such as deglitching, averaging the scans, energy calibration, normalization, background subtraction etc.,²⁰ were performed using the software *ATHENA* of the package *IFEFFIT*.²¹ The normalized component of the EXAFS signal was transformed to k -space and the resultant $\chi(k)$ signal was multiplied by k^3 to emphasise the data at high k . The k^3 -weighted $\chi(k)$ signal was then Fourier transformed and left uncorrected for phase shift. The theoretical $\chi(k)$ was generated by performing *ab-initio* calculations using the code *FEFF8.2*.²² The model function was least-square fitted to the data using the software *ARTEMIS* of the package *IFEFFIT* which uses the algorithm *FEFFIT*.²¹ The fitting parameters involved a single amplitude reduction factor (S_0^2) and an overall energy parameter (ΔE_0) for each data set. A fractional change in the bond length (α_{fit}) was refined for each coordination shell such that a change in the bond length ΔR was given by $\Delta R = \alpha_{fit} \times R_{theory}$. Each coordination shell was assigned a separate mean-squared relative displacement parameter (σ^2) depending on the type of atoms it contained and its mean distance from the central absorber. The parameters for multiple scattering paths were constrained in terms of those of corresponding single scattering paths.²³ Various statistical parameters such as χ^2 , reduced chi-square (χ_v^2) and the R -factor were used to assess the quality of an EXAFS fit. However, since χ^2 and χ_v^2 are evaluated based on measurement uncertainties and *FEFFIT* poorly estimates the true measurement uncertainties,^{23–25} both these parameters do not reflect the true quality of the fit. Nevertheless, both χ^2 and χ_v^2 were used to assess which model fits best the data. The statistical quality of the fit was given by its R -factor which is independent of measurement uncertainties.^{23–25} A fit with an R -factor less than 0.02 (i.e. 98 % agreement between data and theory) is considered to be a good fit.^{23–25}

Results

As shown in Figure 1a, the cell delivered a specific capacity of 388 mAh/g when charged to 5 V and of 200 mAh/g when discharged to 2 V with a 1st cycle efficiency of ~ 50 % (Figure 1b). The long plateau above 4.5 V vs. Li/Li⁺ during the 1st charge that delivers most of the capacity is a characteristic of Li₂MnO₃^{13–15,18,26} and Li₂MnO₃-containing cathode materials.^{1–9} The capacity delivered during the 1st charge (i.e. activation) depends on the rate at which the cell is charged. However, the capacity during subsequent cycles is independent of the rate. Therefore, the cell was first-charged to 5 V using C/50, while subsequent cycling was carried out at C/10. As shown in Figure 1b, the electrochemical performance of Li₂MnO₃ degrades upon cycling. During the 33rd cycle, the cell delivers a specific capacity of ~ 110 mAh/g both during charge and discharge, which is just ~ 55 % of that of the 1st discharge.

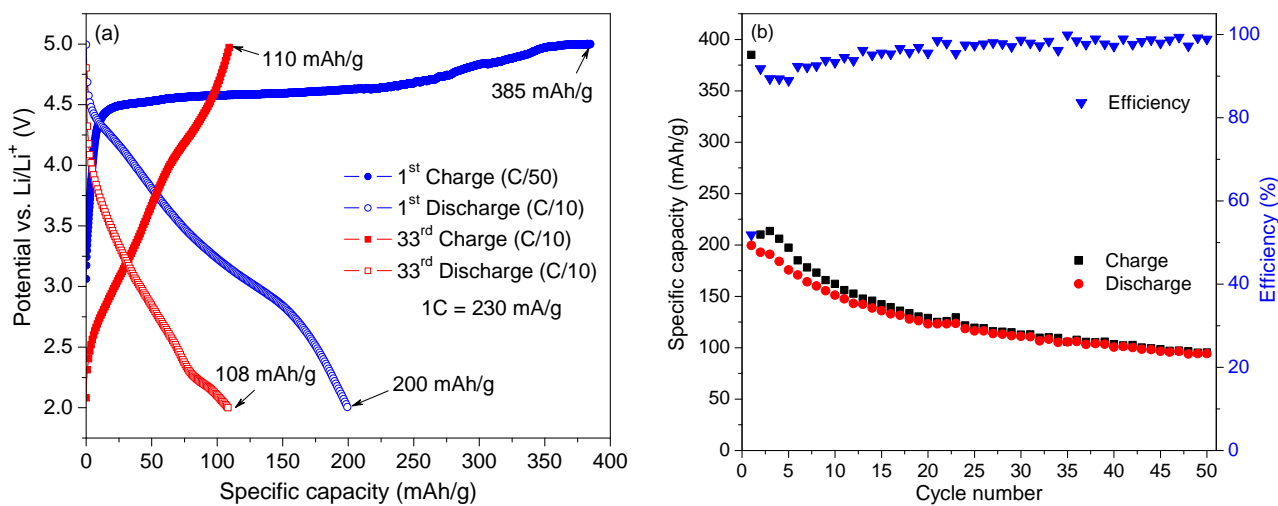


Figure 1: (a) Charge-discharge profiles of Li₂MnO₃ when cycled between 2.0 V and 5.0 V during the 1st and 33rd cycles and (b) Charge-discharge capacities obtained during each cycle along with the electrochemical efficiency.

XANES

As shown in Figure 2a, the absorption edge is characterized by a variety of edge-features such as, (1) an absorption threshold (or the first peak in the derivative spectrum, not shown), (2) a $1s \rightarrow 3d$

transition, corresponding to the pre-edge peak, (3) the main edge, corresponding to the vertically rising portion of the edge (or the second peak in the derivative spectrum, not shown) and (4) a $1s \rightarrow 4p$ transition, corresponding to the maximum of the vertically rising portion of the edge.²⁷ A relative shift in the position of these features, often called a chemical shift, provides an empirical mean for the estimation of the average valence state of the central absorbing atom. The inset in Figure 2a shows an enlarged pre-edge region of these spectra. In order to enhance the visibility of the pre-edge peaks of other reference compounds, the intense pre-edge peak of KMnO_4 is omitted from the inset. The pre-edge regions of MnO , MnO_2 and KMnO_4 are characterized by a single $1s \rightarrow 3d$ peak, while for Mn_2O_3 this peak is split into two, poorly resolved t_{2g} and e_g peaks. For LiMn_2O_4 , this peak splitting is better resolved. The intensity of the pre-edge peak is minimum for MnO , intermediate for MnO_2 and maximum for KMnO_4 .

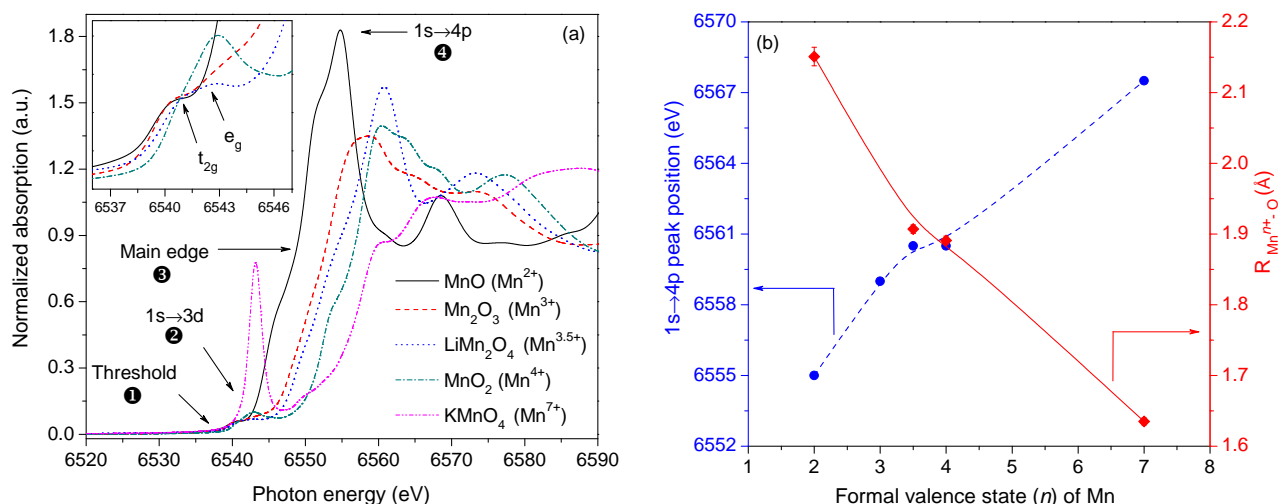


Figure 2: (a) Normalized absorption spectra for various manganese reference compounds with the inset showing an enlarged pre-edge region of four compounds and (b) Variation in the position of the $1s \rightarrow 4p$ peak (dashed blue line) and the average metal-ligand bond length (solid red line) for these compounds.

Inner d -orbitals are more tightly bound and, therefore, less sensitive to chemical changes than loosely bound outer p -orbitals. Thus, chemical shifts observed at the position of the $1s \rightarrow 4p$ peak are more pronounced than those observed at any other features.^{27,28} As a result, chemical shifts are interpreted in terms of the position of the $1s \rightarrow 4p$ peak. Figure 2b shows that with increasing formal valence state of Mn the position of this peak moves to higher energy and the average metal-ligand

bond length decreases. The reported values of bond lengths are obtained by fitting the EXAFS data of individual reference compounds (refer to Figure 13 and Table 1 in Supp.Info.).

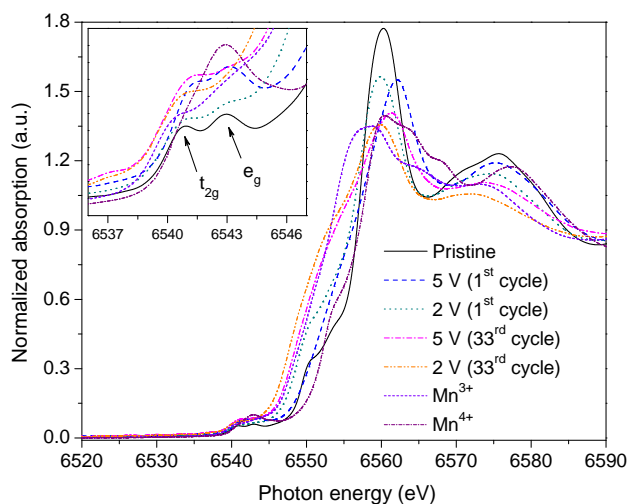


Figure 3: Normalized absorption spectra for various Li_2MnO_3 samples along with those of Mn^{3+} and Mn^{4+} reference compounds. The inset shows an enlarged pre-edge region.

As shown in Figure 3, the absorption spectra for various Li_2MnO_3 samples appear more complex than those of manganese reference compounds due to the presence of several points of intersection along the main edge where some of the spectra cross. Closer examination of these spectra reveals that the trend in chemical shifts varies widely before and after these intersection points. As shown in the inset, the pre-edge region in the pristine state is characterized by a splitting of Mn $3d$ orbitals into t_{2g} and e_g orbitals. As the cathode is charged to 5 V, the intensity of the pre-edge peak increases and the peak splitting becomes less clear. When the cathode is discharged to 2 V, the intensity of the pre-edge peak decreases. For the cycled samples, changes in the pre-edge region are less obvious.

EXAFS

The comparison between the $\chi(k)$ signals of various Li_2MnO_3 samples in Figure 4a reveals that the EXAFS oscillations are reduced as soon as the cathode is charged to 5 V. In the corresponding Fourier transforms in Figure 4b, this is reflected by a preferential reduction in the amplitude of the

1st shell of O atoms besides an overall damping of other shells. Qualitatively, $\chi(k)$ of the cycled-charged sample (i.e. the sample charged to 5 V during the 33rd cycle) appears similar to that of the sample charged during the 1st cycle, except that the signal is further damped. Besides clear reduction in the peak amplitudes, the higher order shells of Mn atoms (at ~ 4.7 Å) and O atoms (at ~ 5.3 Å) largely disappear upon cycling.

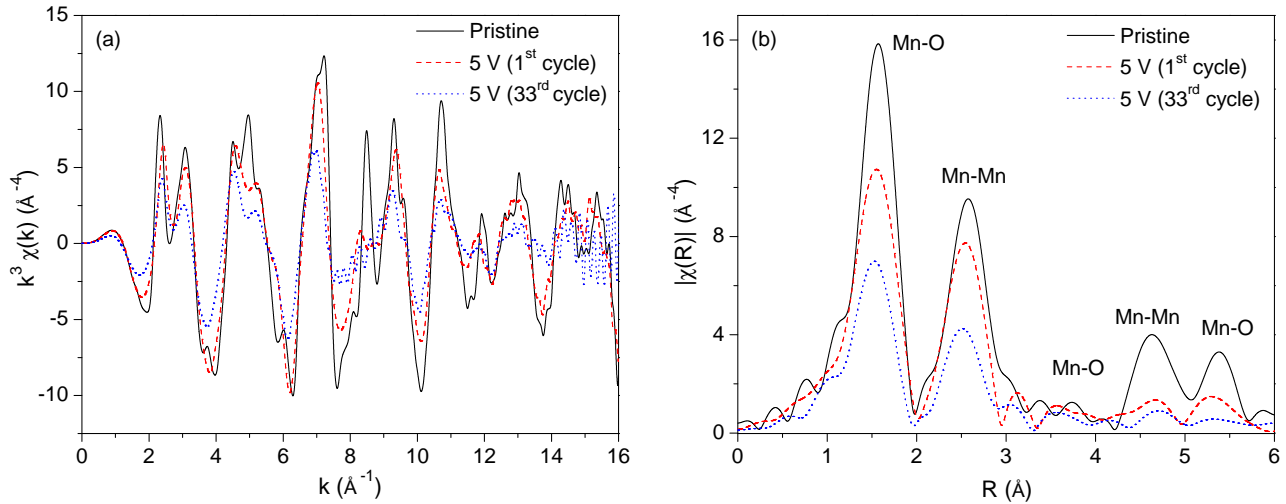


Figure 4: (a) k^3 -weighted $\chi(k)$ signals and (b) their Fourier transforms for Li_2MnO_3 samples in the pristine state (solid black line), when charged to 5 V during the 1st cycle (dashed red line) and when charged to 5 V during the 33rd cycle (dotted blue line).

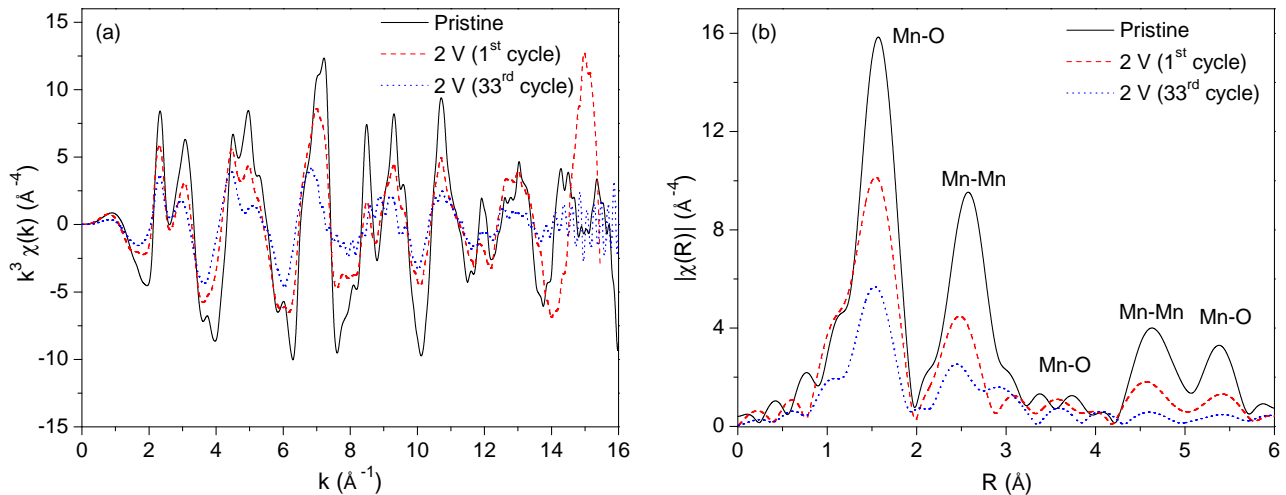


Figure 5: (a) k^3 -weighted $\chi(k)$ signals and (b) their Fourier transforms for Li_2MnO_3 samples in the pristine state (solid black line), when discharged to 2 V during the 1st cycle (dashed red line) and when discharged to 2 V during the 33rd cycle (dotted blue line).

As shown in Figure 5a, every feature of the $\chi(k)$ signal corresponding to the pristine sample is reproduced when the cathode is discharged to 2 V during the 1st cycle, however, with reduced amplitudes. This is also indicated by close similarities in their Fourier transforms in Figure 5b. Again, the EXAFS signals corresponding to the cycled-discharged sample (i.e. the sample discharged to 2 V during the 33rd cycle) appear similar to those of the sample discharged during the 1st cycle, however, the higher order shells are damped.

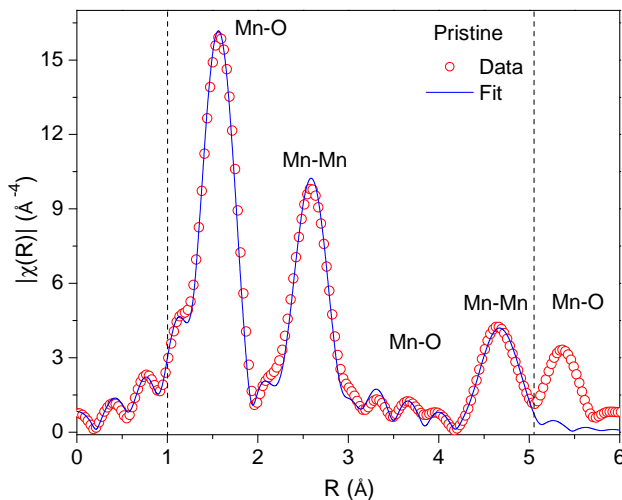


Figure 6: EXAFS fit to the data of Li_2MnO_3 sample in the pristine state. The dotted lines indicate the fitting range.

EXAFS data in the pristine state were fitted by the monoclinic structure of Li_2MnO_3 ($C2/m$)²⁹ (Figure 6). Best-fit parameters are reported in Table 2 (see Supp.Info.). When the number of oxygen nearest neighbors (O_{N-N}) was constrained to that obtained from the theoretical model, the fit refined S_0^2 to 0.76(4) which is consistent with S_0^2 values obtained by fitting the EXAFS data of other manganese reference compounds. Conversely, when S_0^2 was constrained to its nominal value of 0.7, the fit refined O_{N-N} to 6.4(4) which is consistent with the fact that in Li_2MnO_3 Mn^{4+} is octahedrally coordinated by oxygen. In order to refine a physically reasonable value of nearest neighbors it is essential to use a better estimate of S_0^2 since a product of these two parameters determines an overall amplitude of the EXAFS oscillation. In situations where structural changes are to be followed as a result of any physical or chemical change that the sample has undergone, S_0^2 is best estimated from the starting material. From this aspect, S_0^2 determined from the pristine

sample of Li_2MnO_3 was regarded as best estimate since it has known oxygen coordination. The S_0^2 thus determined was constrained when O_{N-N} was to be estimated.

It has been reported that Li extraction from Li_2MnO_3 occurs with a simultaneous loss of oxygen, giving rise to the formation of a layered MnO_2 -type structure (trigonal, $R\bar{3}m$) with the average valence state of Mn remaining unchanged at 4+.¹¹ There are also reports claiming the formation of either layered MnO_2 -type structure or α - MnO_2 -type structure (tetragonal, $I4/m$) upon chemical delithiation of Li_2MnO_3 .^{30,31} In order to assess such reports, EXAFS data of the sample charged to 5 V during the 1st cycle were fitted using the crystal structures of α - MnO_2 and layered MnO_2 . The best fit was obtained assuming the layered MnO_2 structure (Figure 7a). Best-fit parameters are reported in Table 3 (see Supp.Info.).

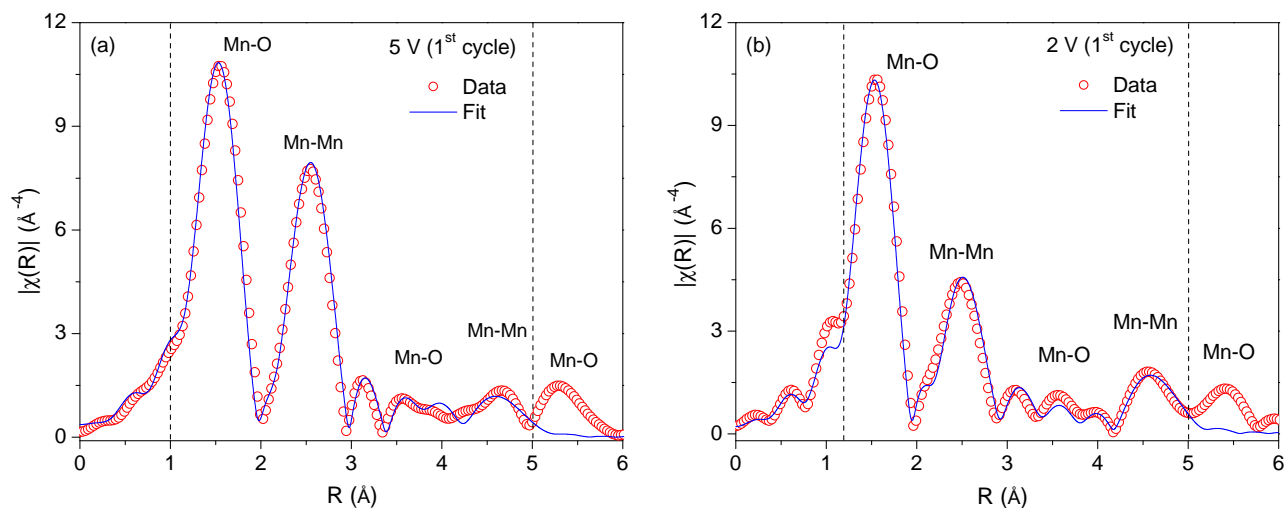


Figure 7: EXAFS fits to the data of Li_2MnO_3 samples (a) When charged to 5 V and (b) When discharged to 2 V during the 1st cycle.

It has been proposed that Li re-insertion into layered MnO_2 occurs with a simultaneous reduction of Mn^{4+} to Mn^{3+} , thus forming LiMnO_2 .^{6,32} Therefore, an attempt was made to fit the EXAFS data of the sample discharged to 2 V during the 1st cycle by a layered MnO_2 structure. However, there was no agreement between the data and theory. The data were rather explained by a Li_2MnO_3 structure when O_{N-N} was allowed to vary in the fit while constraining S_0^2 to 0.7 (Figure 7b). Best-fit parameters are reported in Table 4 (see Supp.Info.). Note that O_{N-N} has reduced from 6 in the pristine state to 4.6(5) in the discharged state.

Various reports have claimed that prolonged cycling of Li_2MnO_3 gives rise to the formation of a spinel-like phase.^{14,26,32} Therefore, an attempt was made to fit the data of the cycled samples using crystal structures of various candidate spinel phases such as LiMn_2O_4 , $\text{Li}_2\text{Mn}_4\text{O}_9$ and $\text{Li}_4\text{Mn}_5\text{O}_{12}$. Again, there was no agreement between the data and theory. For comparison, the EXAFS data of one of the spinel phases LiMn_2O_4 is shown in Figure 8.

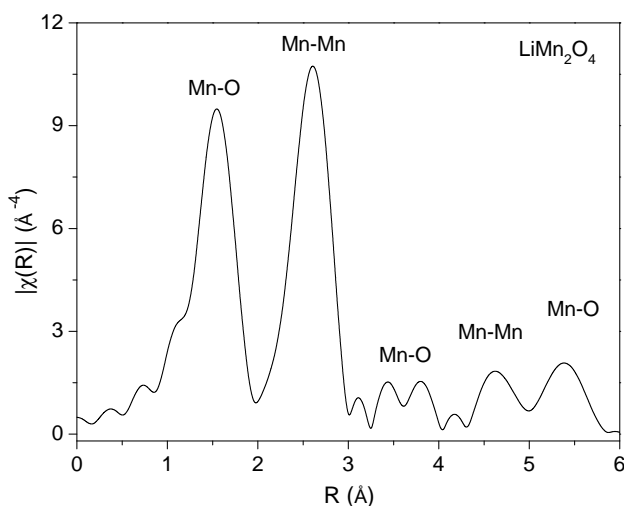


Figure 8: EXAFS data of LiMn_2O_4 spinel.

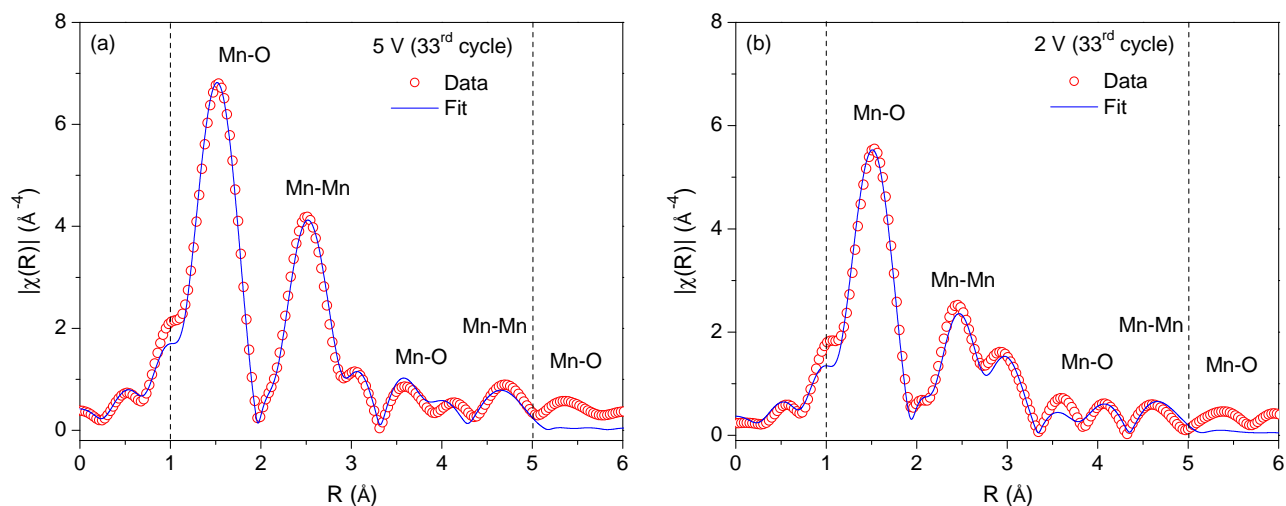


Figure 9: EXAFS fits to the data of Li_2MnO_3 samples (a) When charged to 5 V and (b) When discharged to 2 V during the 33rd cycle.

Qualitatively, the EXAFS data of the cycled samples appear similar to those of their counterparts during the 1st cycle. As a result, a layered MnO_2 structure was assumed to fit the data of the

cycled-charged sample. When O_{N-N} was constrained to 6, the fit refined S_0^2 to 0.43(3), which is smaller than for the Mn absorber. Conversely, when S_0^2 was constrained to 0.7, the fit refined O_{N-N} to 3.6(4), which is very low considering the weak pre-edge peak of the cycled samples (inset in Figure 3), suggesting octahedral coordination. These fit results emphasise the effect of an observed reduction in the EXAFS signals upon cycling. A gradually declining electrochemical performance of the cell upon cycling (Figure 1b) suggests a gradual decrease in the intercalation ability of the active material. Therefore, a parameter describing an effective concentration of the active material, X_{eff} , was introduced to the model and the data refitted. A fit constraining S_0^2 to 0.7 and O_{N-N} to 6, refined X_{eff} to 0.61(5) (see Table 5 in Supp.Info.) with a good agreement with the data as shown in Figure 9a. Similarly, the EXAFS data of the cycled-discharged sample were explained by a Li_2MnO_3 structure (Figure 9b). A fit constraining X_{eff} to 0.6 and S_0^2 to 0.7 refined O_{N-N} to 4.6(5) (see Table 6 in Supp.Info.).

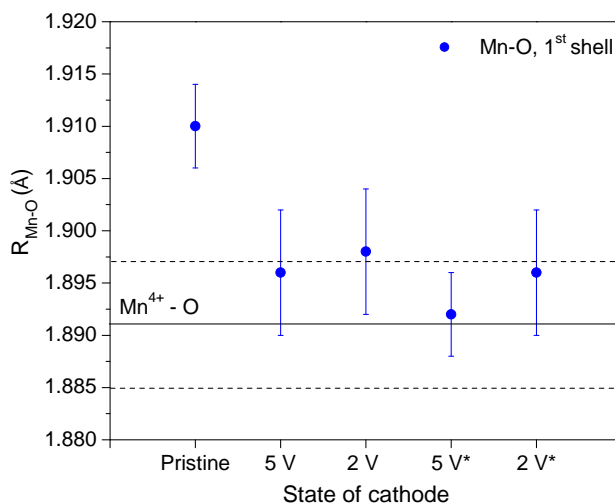


Figure 10: Comparison of the metal-ligand bond length for the electrochemically cycled Li_2MnO_3 samples during the 1st and 33rd cycles. The asterisk (*) represents the charged-discharged samples during the 33rd cycle. The solid line indicates the average Mn^{4+} -O bond length obtained by fitting the EXAFS data of MnO_2 reference compound and dotted lines indicate statistical uncertainties of the fitted value.

A comparison between the metal-ligand bond length of various Li_2MnO_3 samples is shown in Figure 10. The average Mn-O bond length in the pristine state is slightly higher than that of Mn^{4+} -O. As the cathode is charged to 5 V, this bond length shortens and becomes similar to that

of $\text{Mn}^{4+}\text{-O}$. The bond length, however, remains unchanged during subsequent cycling.

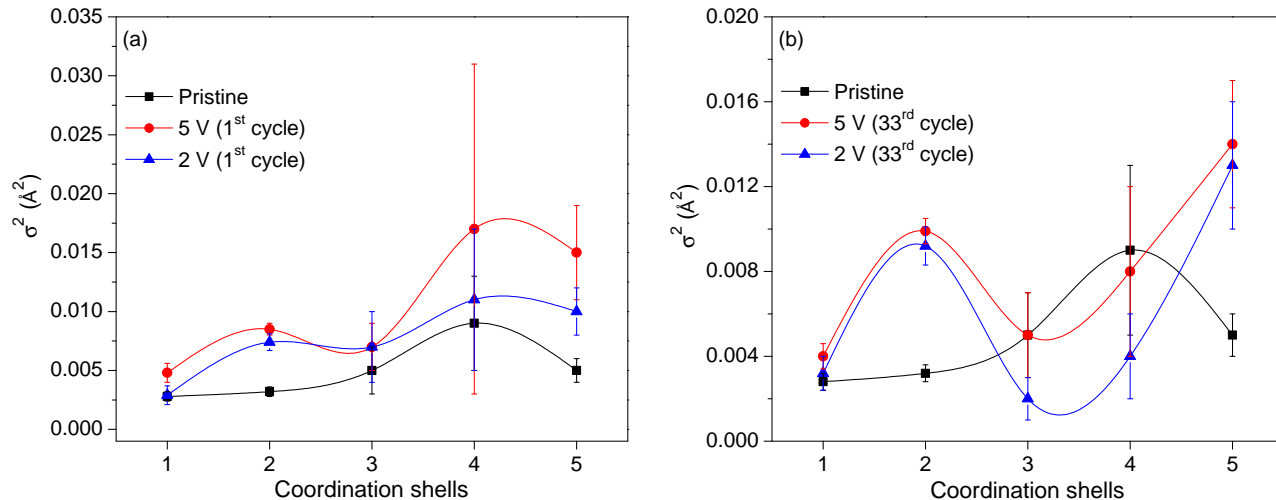


Figure 11: Structural disorder in charged-discharged samples of Li_2MnO_3 (a) During the 1st cycle and (b) During the 33rd cycle.

σ^2 is the distribution of the backscattering atoms around their mean position measured with respect to the central absorbing atom. This distribution can be either caused by thermal vibrations (thermal disorder) or by static displacement of atoms (structural disorder).^{33,34} Since all samples in the present study are characterized at the same temperature (i.e. room temperature), a systematic variation in their σ^2 can be attributed to structural disorder introduced in the material as a result of electrochemical cycling, while neglecting thermal disorder. As shown in Figure 11a, the pristine sample exhibits the smallest, while the charged sample exhibits the largest disorder for all shells during the 1st cycle. The structural disorder for the discharged sample is intermediate and in fact, appears to revert back to that of the pristine state. Note that σ^2 associated with the 4th shell is particularly large and ill-refined for the charged sample, while it is small and better refined for the discharged sample. The structural disorder associated with the cycled samples is shown in Figure 11b. The cycled-charged sample has larger disorder than the cycled-discharged sample for all shells. However, the trend is less clear beyond the 2nd shell.

The statistical EXAFS fit parameters for various Li_2MnO_3 samples are reported in Table 7 (see Supp.Info.). A good agreement between the data and theory for all samples can be seen by their R-factors that are < 0.02 .

Discussion

XANES

$1s \rightarrow 3d$ transitions are forbidden by dipole rules in centrosymmetric configurations such as in regular octahedral symmetry. However, with increasing distortion from ideal octahedral symmetry, the probability of a transition to d -orbitals increases. For tetrahedral symmetry, the metal-ligand orbital intermixing results in dipole-allowed $1s \rightarrow 3d$ transitions with an intense pre-edge peak.^{28,35} As shown in Figure 2a, MnO with perfect octahedral symmetry has the lowest pre-edge peak intensity. As the distortion in octahedral symmetry increases in the order Mn_2O_3 ³⁶ \rightarrow LiMn_2O_4 ³⁷ \rightarrow MnO_2 ,³⁸ the intensity of the pre-edge peak increases correspondingly. KMnO_4 with tetrahedral symmetry³⁹ has the highest pre-edge peak intensity. Moreover, MnO with Mn^{2+} exhibits the longest Mn-O bond length, while KMnO_4 with Mn^{7+} has the shortest Mn-O bond length among all manganese reference compounds. Thus, the strength of the pre-edge peak can be correlated to the local coordination symmetry around the absorbing atom and the average metal-ligand bond length.

The metal-ligand bond length determines the extent to which orbital intermixing takes place. As a result of this intermixing, the repulsive forces between the electrons increase the energies of these orbitals. Thus, metal d -orbitals split into t_{2g} and e_g orbitals.^{28,35} This can be realized by observing the pre-edge peaks of various manganese reference compounds (inset in Figure 2). MnO is a model octahedral compound, thus showing a very faint pre-edge peak. A higher valence state of Mn in Mn_2O_3 implies a shorter average Mn-O bond length than in MnO, which leads to higher electronic repulsions and higher orbital energies. As a result, the onset of pre-edge peak splitting in the Mn_2O_3 spectrum is clearly visible. This peak splitting becomes more pronounced with a further increase in the average valence state of Mn to $\text{Mn}^{3.5+}$ or shortening of the average Mn-O bond length in LiMn_2O_4 . For Li_2MnO_3 , where Mn^{4+} is octahedrally coordinated by O^{2-} ,⁴⁰ the peak splitting is maximum and best resolved (inset in Figure 3), as has been reported previously.^{18,41} A similar peak splitting phenomenon is also observed at the Fe K-edge of LiFePO_4 ,^{28,35} and is often known as crystal field splitting.

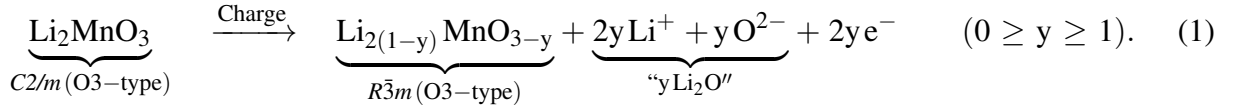
Empirically, a chemical shift in the absorption spectra can be correlated to the formal valence state of an absorbing atom.^{27,42} However, besides the valence of an absorbing atom, chemical shifts are also affected by other structural features such as type, symmetry and number of nearest neighbors, character of bond etc.²⁷ Also, the extent to which each of these features contribute to the chemical shift varies widely from material to material. The observed unambiguous chemical shift for various manganese reference compounds in Figure 2a is the simplest example. However, for the samples of interest determining the chemical shift can be quite complex. For instance, it is difficult to judge the chemical shift among various Li_2MnO_3 samples in Figure 3 since there are several points along the main edge where spectra cross. In this situation, an estimation of the valence state depends on the reference point chosen. Thus, the approach involving the determination of the valence state of an absorbing atom from the observed chemical shift is strictly empirical, highly subjective^{18,26} and sometimes confusing.⁴¹ Contrary to this, the average metal-ligand bond length obtained by fitting the EXAFS data provides more reliable information about the valence state of an absorbing atom since this bond length primarily depends on the ionic radius of the absorbing atom and, in turn, on its valence state as demonstrated in Figure 2b.

EXAFS

Structural changes during the 1st charge

XAS can distinguish between different atom types based on their ability to scatter the ejected photoelectron, which in turn depends on their atomic number Z . Despite Mn ($Z=25$) having a higher atomic number than O ($Z=8$), the amplitude of the signal coming from the 1st shell of O atoms is higher than from the 2nd shell of Mn atoms in Li_2MnO_3 (Figure 6). This can be attributed to a higher overall concentration of $\frac{O}{Mn}$ atoms (i.e. O:Mn=3:1) and an ordered structure of Li_2MnO_3 resulting in six O atoms in the 1st shell, but only three Mn atoms in the 2nd shell (see Table 2 in Supp.Info.). Thus, the ratio of the amplitudes of the first two Fourier transform peaks, i.e. the $\frac{Mn-O}{Mn-Mn}$ ratio, being > 1 is the EXAFS signature reflecting the atomic arrangements of the Li_2MnO_3 structure.

A preferential reduction in the amplitude of the 1st shell of O atoms besides an overall damping of other shells at 5 V (Figure 4b) is consistent with previous reports,¹⁸ and can be attributed, respectively, to the oxygen loss and structural disorder introduced thereby upon Li extraction. This can be explained by the fact that the best fit to the EXAFS data at 5 V (Figure 7a) is based on a layered MnO₂ structure, which has not only a reduced concentration of $\frac{O}{Mn}$ atoms but is also a disordered form of Li₂MnO₃.¹⁴ An increase in the σ^2 value for each coordination shell of the charged sample (Figure 11a) further confirms the disorder introduced into the material by Li extraction. Consistent observation has been reported in the form of a loss of superlattice reflections in the XRD pattern of Li₂MnO₃ upon Li extraction.¹⁸ Thus, Li extraction occurs with a concurrent removal of oxygen through its oxidation according to⁴³ :



Fitting the EXAFS data of the charged sample refined O_{N-N} to 6.1(6) (see Table 3 in Supp.Info.), which suggests that despite oxygen removal, overall octahedral symmetry around Mn atoms is maintained. This is confirmed by similarities in the pre-edge region of the pristine and charged samples (inset in Figure 3). However, the pre-edge peak for the charged sample is more intense and peak splitting is less clear than for the pristine sample, which indicate a change in the arrangements of O atoms as nearest neighbors around the central Mn atom upon Li extraction. The observed shortening of the average Mn-O bond length upon charge (Figure 10) can be attributed to these atomic rearrangements. Consistent observations have been reported in the form of a lattice contraction upon Li extraction from Li₂MnO₃.^{18,32} Thus, both XANES and EXAFS results confirm the atomic rearrangements in the material as a result of oxygen loss which give rise to the formation of a layered MnO₂-type structure.

Despite this structural modification, the $\frac{Mn-O}{Mn-Mn}$ ratio remains > 1 for the charged sample (Figure 7a), which suggests that the material retains its original Li₂MnO₃-like character even upon Li

extraction. Thus, Li extraction does not completely destroy the ordering of Li and Mn within the $[\text{Li}_{1/3}\text{Mn}_{2/3}]\text{O}_2$ slabs,³² and that not all the extracted charge corresponds to oxygen release only. Partial oxidation of oxygen anions can also supply electrons to the external circuit without releasing oxygen from the material.^{41,44–46} Similarly, electrolyte oxidation^{47–49} can also contribute to the observed charge capacity during activation. It is possible that H^+ generated as a result of electrolyte oxidation could replace electrochemically extracted Li^+ in the structure.^{13–15,32,43} A similar $\text{Li}^+ - \text{H}^+$ exchange mechanism has been observed for lithium manganese oxide spinels.^{50,51}

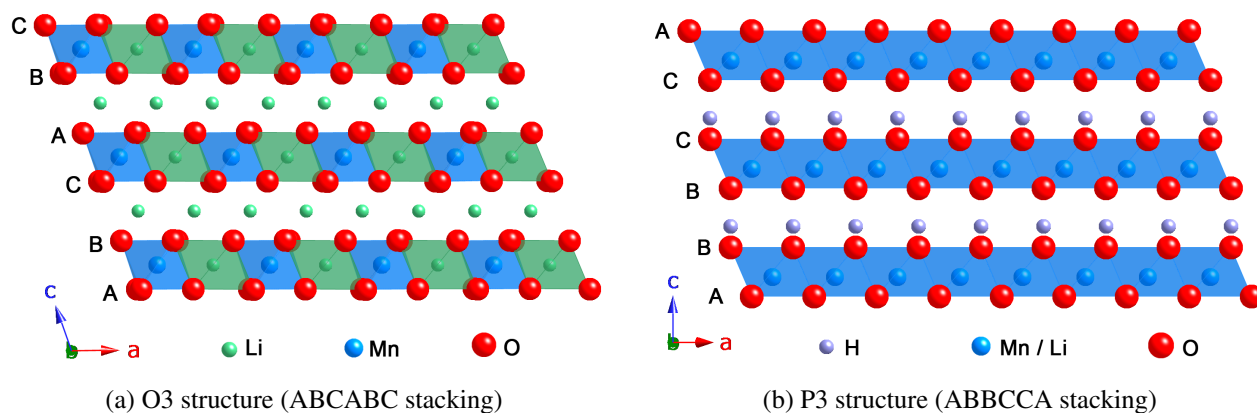
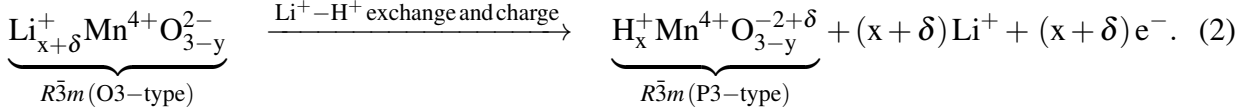


Figure 12: Stacking sequence of close-packed oxygen layers in (a) O3 structure of Li_2MnO_3 ($C2/m$)²⁹ and (b) P3 structure ($R\bar{3}m$) of proton-exchanged material.⁵² Note that O-H-O bonds are asymmetric in P3 structure.

The $\text{Li}^+ - \text{H}^+$ exchange mechanism is also supported in Li_2MnO_3 by the observed change in the stacking sequence of oxygen layers from O3-type (ABCABC) to P3-type (ABBCCA) due to the presence of protons in the interslab region and strong O-H-O bonding.^{14,32} For comparison, O3-type and P3-type structures are shown in Figure 12. The ordered atomic arrangements of O3 structure in the pristine state produced well-defined Fourier transform peaks between 3 - 4.2 Å in Figure 6. These peaks correspond to O atoms located at the boundaries of the neighboring $[\text{Li}_{1/3}\text{Mn}_{2/3}]\text{O}_2$ slabs and are separated by interslab Li atoms (Figure 12a). For the charged sample, these peaks are replaced by a broad diffuse structure (Figure 7a). Correspondingly, σ^2 associated with the 4th shell, which represents O atoms of the neighboring slabs increases abruptly and remains ill-refined upon charge (Figure 11a). Both, smeared EXAFS peaks and large ill-refined

σ^2 suggest a large static displacement in the position of O atoms of the neighboring slabs and, in turn, confirm a change in the stacking sequence of oxygen layers. Thus, the presence of H^+ in the interslab region, as a result of $Li^+ - H^+$ exchange, shears the oxygen layers due to strong O-H-O bonding and alters their stacking sequence from O3-type to P3-type according to :



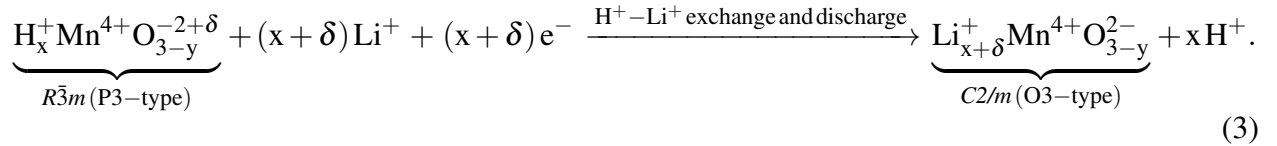
Structural changes during the 1st discharge

Several reports have claimed that Li re-insertion into layered MnO_2 gives rise to the formation of $LiMnO_2$ with the concurrent reduction of Mn^{4+} to Mn^{3+} .^{6,32} According to these reports, the local structure of the discharged sample should be identical to that of the charged sample and the proposed reduction of Mn^{4+} to Mn^{3+} should be accompanied by an increase in the average Mn-O bond length. Contrary to these, the EXAFS data of the discharged sample (Figure 7b) appear identical to those of the pristine sample (Figure 6), however, with reduced amplitudes and the average Mn-O bond length remains unchanged from that of the charged sample (Figure 10). Both these results contradict the proposed hypothesis about Li re-insertion into layered MnO_2 . A specific discharge capacity of 200 mAh/g during the 1st cycle (Figure 1a) suggests that a significant amount of Li is re-inserted into the material. This could have happened by exchanging already present H^+ in the structure with Li^+ .¹⁴ Discharge could then involve the reduction of partially oxidized oxygen anions,^{41,44-46} and possibly that of electrolyte species which could consume H^+ driven out of the material.¹⁴

Qualitative similarities between the EXAFS data of the pristine and discharged samples suggest structural re-ordering upon Li re-insertion. This is consistent with a reduction in the σ^2 value for the coordination shells of the discharged sample (Figure 11a). However, since permanent disorder caused by oxygen removal cannot be reverted, the discharged sample exhibits slightly higher disorder than the pristine sample. Due to this and despite qualitative similarities, the EXAFS

amplitudes for the discharged sample are slightly reduced than those of the pristine sample. The value of O_{N-N} refined to 4.6(5) for the discharged sample (Table 4 in Supp.Info.) should not be interpreted as tetrahedral coordination around Mn atoms, since the pre-edge region for the discharged sample is characterized by a weak pre-edge peak quite similar to that of the pristine sample (inset in Figure 3) rather suggesting octahedral coordination. Therefore, O atoms within MnO_6 octahedra acquire similar arrangements as in the pristine state upon discharge, however, there are O vacancies in some of these octahedra.

The Fourier transform peaks between 3 - 4.2 Å representing O atoms of the neighboring slabs reappear upon discharge (Figure 7b). Correspondingly, σ^2 associated with these O atoms (4th shell) decreases (Figure 11a). Both these results suggest a change in the stacking sequence of oxygen layers from P3-type back to the original O3-type and are in good agreement with an earlier report of Rossouw et al.⁵³ where the XRD pattern of a re-lithiated sample closely resembled that of the parent Li_2MnO_3 . Thus, Li re-insertion indeed occurs by exchanging already present protons in the structure which reverts the stacking sequence of oxygen layers from P3-type back to the original O3-type according to :



The resultant structure is similar to that of the parent Li_2MnO_3 , except that it contains less Li and O. The driving force for such a structural reversion is believed to be the relaxation of strained oxygen layers caused by displacing H^+ in the interslab region by Li^+ .

Structural changes upon cycling

It has been claimed that prolonged cycling of Li_2MnO_3 gives rise to the formation of a spinel-like phase.^{14,26,32} This claim is further supported by qualitative similarities between the electrochemical profiles of cycled Li_2MnO_3 and $LiMn_2O_4$ spinel¹⁴ and the fact that the formation of a spinel-

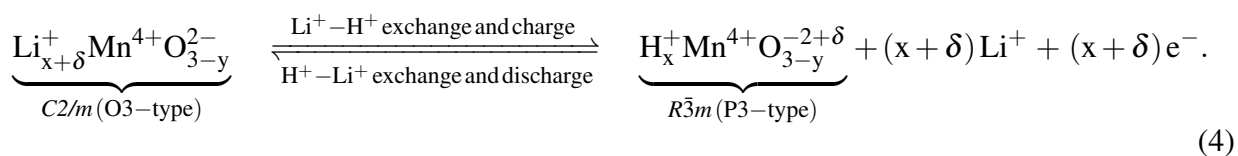
like phase from layered LiMnO_2 that presumably forms during the 1st discharge is favored.^{54,55} However, the EXAFS data of the discharged sample (Figure 7b) clearly suggest that Li re-insertion into layered MnO_2 gives rise to the formation of Li_2MnO_3 -type structure. This result is in conflict with the existing hypothesis and raises doubts about the formation of a spinel-like phase upon cycling. The crystallographic difference between layered Li_2MnO_3 and spinel LiMn_2O_4 gives rise to distinct EXAFS signals (see Figure 6 and Figure 8). A major difference lies in their $\frac{\text{Mn}-\text{O}}{\text{Mn}-\text{Mn}}$ ratios. Based on this criterion, the local structure of the cycled samples (Figure 9) is more similar to their counterparts during the 1st cycle (Figure 7) than to LiMn_2O_4 .

Higher order shells of Mn atoms (at ~ 4.7 Å) and O atoms (at ~ 5.4 Å) clearly visible during the 1st cycle are reduced during the 33rd cycle (see Figure 4b and Figure 5b). These shells represent Mn and O atoms from the neighboring $[\text{Li}_{1/3}\text{Mn}_{2/3}]\text{O}_2$ slabs. The formation of a spinel-like phase, if any, does not explain the observed reduction in EXAFS signals which should rather express an increased level of structural disorder in the material upon cycling. The best fit to the EXAFS data of the cycled-charged sample is by a layered MnO_2 structure and refined the fraction of active material (X_{eff}) to 0.61(5) (Table 5 in Supp.Info.). This is in good agreement with the fact that charge-discharge capacities during the 33rd cycle are ~ 55 % of that of the 1st discharge. Similarly, the best fit to the EXAFS data of the cycled-discharged sample is by a Li_2MnO_3 structure and refined O_{N-N} to 4.6(5) (Table 6 in Supp.Info.). This is consistent with the value obtained during the 1st discharge.

These results lead us to two major conclusions. First, the structural changes during the 33rd cycle are similar to those observed during the 1st, however, the effective concentration of active material is reduced to 61(5) % up to the 33rd cycle. Second, oxygen removal occurs only during activation of the material in the 1st cycle. This is confirmed by the weak pre-edge peak of the cycled samples (inset in Figure 3), consistent with octahedral coordination around Mn atoms. As observed during the 1st cycle, structural disorder for the cycled-charged sample is higher than for the cycled-discharged sample (Figure 11b). However, the trend is less clear beyond the 2nd shell. Note that the structural “visibility” for the cycled samples is also limited to the first two shells as

indicated by well-defined Fourier transform peaks. These results suggest that atomic arrangements within an individual $[\text{Li}_{1/3}\text{Mn}_{2/3}]\text{O}_2$ slab are intact. However, the stacking sequence of subsequent slabs is disturbed upon cycling.

The average Mn-O bond length for the cycled samples (Figure 10) remains unchanged from that of $\text{Mn}^{4+}\text{-O}$, which rules out the conventional charge compensation mechanism involving the $\text{Mn}^{3+}/\text{Mn}^{4+}$ redox reaction. Therefore, the observed charge-discharge capacities during subsequent cycles must have different origins such as the participation of oxygen anions in redox processes^{41,44-46} in addition to the repetitive, irreversible oxidation of electrolyte species. During each subsequent charge, electrons are supplied to the external circuit partly by the oxidation of oxygen anions without releasing oxygen from the material and partly by electrolyte oxidation. Protons generated as a result of electrolyte oxidation replace electrochemically extracted Li in the structure. The presence of protons in the interslab region and strong O-H-O bonding alter the stacking sequence of oxygen layers from O3-type to P3-type according to :

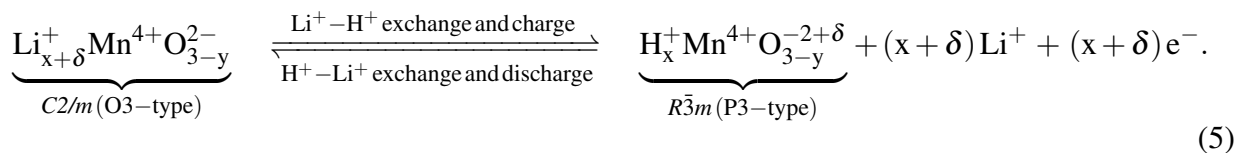


During subsequent discharge, partially oxidized oxygen anions along with electrolyte species are reduced and Li re-insertion occurs by replacing already present protons in the material. Such an exchange reverts the oxygen stacking sequence from P3-type back to the original O3-type. Thus, there is repetitive shearing of oxygen layers during each subsequent cycle which develops enough stresses to cause permanent structural damage. The observed cleavage in Li_2MnO_3 particles along the (001) plane⁴³ can now be explained in terms of shearing of individual $[\text{Li}_{1/3}\text{Mn}_{2/3}]\text{O}_2$ slabs due to a change in their stacking sequence. Moreover, the cycling curve of Li_2MnO_3 in Figure 1b does not show any plateau where fading levels off and at which the electrochemical performance of Li_2MnO_3 corresponds to that of LiMn_2O_4 . In fact, fading starts right from the 1st cycle and continues even beyond the 33rd cycle. This suggests a continuous structural degradation during

cycling. Since the suggested $\text{Li}^+ - \text{H}^+$ exchange mechanism involves the repetitive consumption of electrolyte species, it would inevitably deteriorate the cell performance on the long term. However, the presented results clearly suggest that the capacity degradation is more likely to be caused by the structural degradation of active material rather than the dry-out of electrolyte.

Conclusions

Both XANES and EXAFS provide complementary information that helps to understand structural changes in Li_2MnO_3 . The total charge capacity during activation can be attributed to the oxidation of oxygen anions and that of electrolyte. The concurrent removal of oxygen along with Li gives rise to the formation of a layered MnO_2 -type structure, while maintaining a certain degree of Li and Mn ordering within its $[\text{Li}_{1/3}\text{Mn}_{2/3}]\text{O}_2$ slabs. Protons generated as a result of electrolyte oxidation replace electrochemically extracted Li^+ in the structure. The presence of protons in the interslab region shears the oxygen layers due to strong O-H-O bonding and alters their stacking sequence from O3-type (ABCABC) to P3-type (ABBCCA). Li re-insertion into layered MnO_2 occurs by exchanging already present protons and involves the reduction of partially oxidized oxygen anions. The relaxation of strained oxygen layers caused by exchanging interslab protons with Li reverts their stacking sequence from P3-type back to the original O3-type. The resultant structure upon discharge closely resembles the parent Li_2MnO_3 , however, it contains less Li and O. Mn^{4+} does not participate in electrochemical processes and its average valence state remains unchanged at 4+ at all times. Irreversible oxygen release occurs only during activation of the material. During subsequent cycles, electrochemical processes are governed by unusual redox processes of oxygen anions together with the repetitive, irreversible oxidation of electrolyte species :



Li^+ - H^+ exchange during each subsequent charge-discharge involves a structural flip-over between O3-type ($C2/m$) and P3-type ($R\bar{3}m$) by repeated shearing of oxygen layers. These structural changes build enough stresses over a period of time to cause permanent structural damage and are responsible for the deteriorating electrochemical performance of Li_2MnO_3 upon cycling.

Acknowledgement

The authors acknowledge the financial support from Europäischer Fonds für regionale Entwicklung (EFRE) under project BATMAT (No. 200720132/35). RK acknowledges the financial support from the Hans-L. Merkle Stiftung of the Robert Bosch GmbH.

Supporting Information Available

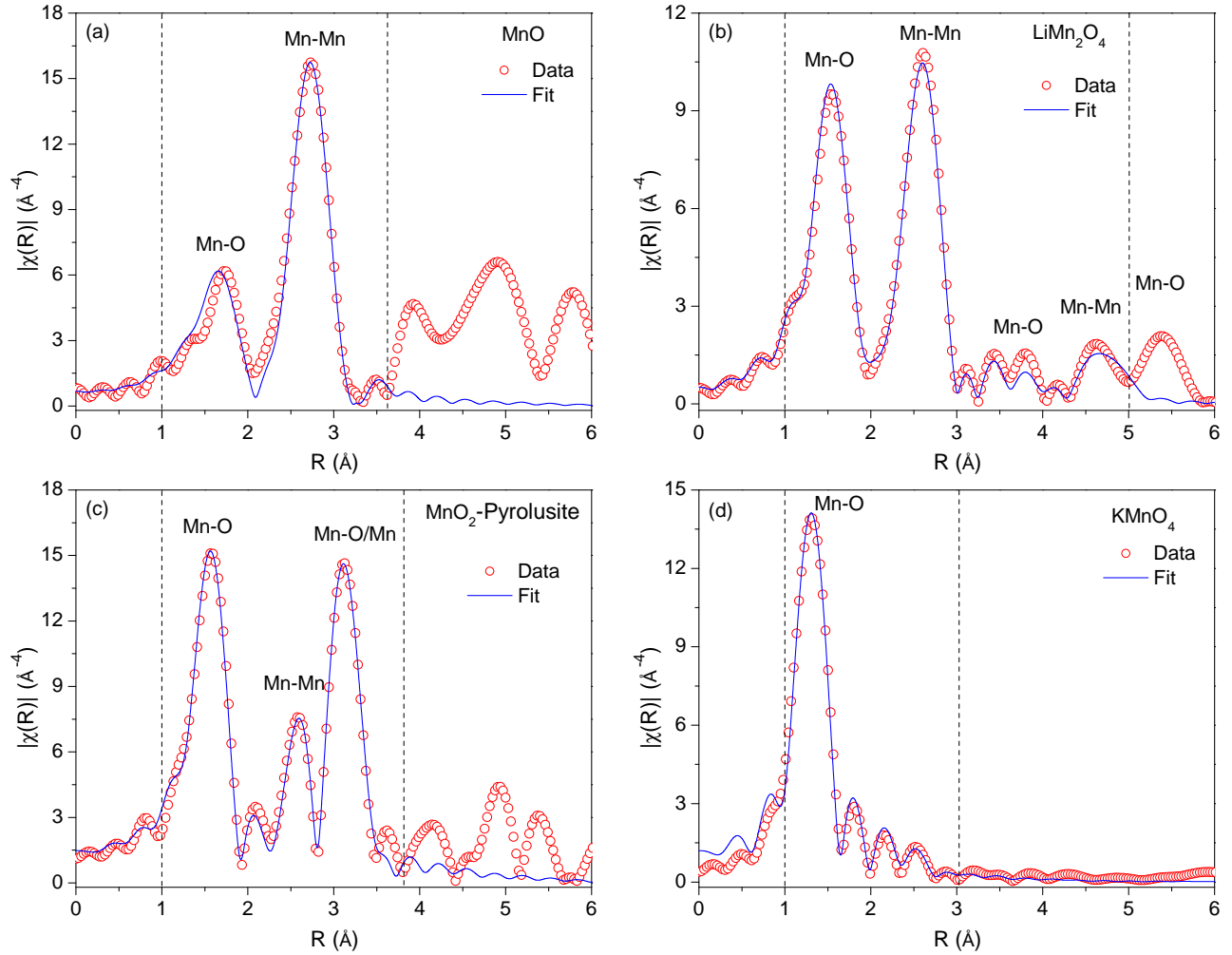


Figure 13: EXAFS fits to the data of various manganese reference compounds.

Table 1: EXAFS fit parameters for the 1st shell of various manganese reference compounds.

Sample	R_{theory} (Å)	α_{fit}	ΔR (Å)	R_{fit} (Å)	R_{mean} (Å)	σ_{fit}^2 (Å ²)
MnO	6×2.222	-0.032 (6)	-0.071 (12)	2.151 (12)	2.151 (12)	0.010 (2)
LiMn ₂ O ₄	6×1.976	-0.035 (3)	-0.069 (6)	1.907 (6)	1.907 (6)	0.0049 (8)
MnO ₂	2×1.878 4×1.891	0.002 (3)	0.004 (6) 0.004 (6)	1.882 (6) 1.895 (6)	1.891 (6)	0.0034 (7)
KMnO ₄	2×1.612 1×1.613 1×1.613	0.014 (3)	0.023 (5) 0.023 (5) 0.023 (5)	1.635 (5) 1.636 (5) 1.636 (5)	1.636 (5)	0.0012 (4)

Table 2: EXAFS fit parameters for Li_2MnO_3 sample in the pristine state. The values in parentheses indicate uncertainties to the least significant digit(s). The parameters without uncertainties were constrained in the fit.

$S_0^2 = 0.76(4)$ $\Delta E_0 = 7.0(7)$						
Path ^a	N_{degen}^b	R_{theory}^c (Å)	α_{fit}	ΔR^d (Å)	R_{fit}^e (Å)	σ_{fit}^2 (Å ²)
Mn-O _{N-N}	2	1.904		-0.002 (4)	1.902 (4)	
	2	1.912	-0.001 (2)	-0.002 (4)	1.910 (4)	0.0028 (4)
	2	1.919		-0.002 (4)	1.917 (4)	
Mn-Mn	2	2.845	0.002 (1)	0.006 (3)	2.851 (3)	0.0032 (4)
	1	2.851		0.006 (3)	2.857 (3)	
Mn-O	2	3.513		0.004 (18)	3.517 (18)	
	2	3.515	0.001 (5)	0.004 (18)	3.519 (18)	0.005 (2)
	2	3.516		0.004 (18)	3.520 (18)	
	2	3.686		0.004 (18)	3.690 (18)	
Mn-O	2	4.388		0.022 (28)	4.410 (28)	
	2	4.390		0.022 (28)	4.412 (28)	
	2	4.395		0.022 (28)	4.417 (28)	
	2	4.578		0.023 (28)	4.601 (28)	
	2	4.579		0.023 (28)	4.602 (28)	
	2	4.587	0.005 (6)	0.023 (28)	4.610 (28)	0.009 (4)
	2	4.594		0.023 (28)	4.617 (28)	
	2	4.599		0.023 (28)	4.622 (28)	
	2	4.638		0.023 (28)	4.661 (28)	
	2	4.672		0.023 (28)	4.695 (28)	
	2	4.693		0.024 (28)	4.717 (28)	
	2	4.721		0.024 (28)	4.745 (28)	
Mn-Mn	4	4.929		0.030 (10)	4.959 (10)	
	2	4.937	0.006 (2)	0.030 (10)	4.967 (10)	0.005 (1)
	2	5.012		0.030 (10)	5.042 (10)	
	2	5.030		0.030 (10)	5.060 (10)	

^a Scattering path from the theoretical model

^b N_{degen} = Degeneracy of scattering paths from the theoretical model

^c R_{theory} = Interatomic distances from the theoretical model

^d $\Delta R = \alpha_{\text{fit}} \times R_{\text{theory}}$

^e $R_{\text{fit}} = R_{\text{theory}} + \Delta R$

Table 3: EXAFS fit parameters for Li_2MnO_3 sample charged to 5 V during the 1st cycle.

$S_0^2 = 0.7$						
$\Delta E_0 = 4.9(1.1)$						
Path	N_{degen}	$R_{\text{theory}} (\text{\AA})$	α_{fit}	$\Delta R (\text{\AA})$	$R_{\text{fit}} (\text{\AA})$	$\sigma_{\text{fit}}^2 (\text{\AA}^2)$
Mn- O_{N-N}	6.1 (6)	1.921	-0.013 (3)	-0.025 (6)	1.896 (6)	0.0048 (8)
Mn-Mn	6	2.816	0.018 (3)	0.051 (9)	2.867 (9)	0.0085 (5)
Mn-O	6	3.409	0.020 (6)	0.068 (22)	3.477 (22)	0.007 (2)
	2	3.661		0.073 (22)	3.734 (22)	
Mn-O	12	4.422	-0.006 (17)	-0.027 (79)	4.395 (79)	0.017 (14)
	12	4.619		-0.028 (79)	4.591 (79)	
Mn-Mn	6	4.878	0.012 (6)	0.059 (30)	4.937 (30)	0.015 (4)
	6	4.959		0.060 (30)	5.019 (30)	

This material is available free of charge via the Internet at <http://pubs.acs.org/>.

Table 4: EXAFS fit parameters for Li_2MnO_3 sample discharged to 2 V during the 1st cycle.

$S_0^2 = 0.7$						
$\Delta E_0 = 2.5 (1.4)$						
Path	N_{degen}	$R_{\text{theory}} (\text{\AA})$	α_{fit}	$\Delta R (\text{\AA})$	$R_{\text{fit}} (\text{\AA})$	$\sigma_{\text{fit}}^2 (\text{\AA}^2)$
Mn-O _{N-N}	4.6 (5)	1.904	-0.003 (3)	-0.006 (6)	1.898 (6)	0.0029 (8)
Mn-Mn	2	2.845	0.005 (3)	0.014 (9)	2.860 (9)	0.0074 (7)
	1	2.851		0.014 (9)	2.865 (9)	
Mn-O	2	3.513	-0.006 (6)	-0.021 (22)	3.492 (22)	0.007(3)
	2	3.515		-0.021 (22)	3.494 (22)	
	2	3.516		-0.021 (22)	3.495 (22)	
	2	3.686		-0.021 (22)	3.664 (22)	
Mn-O	2	4.388	0.006 (9)	0.026 (42)	4.414 (42)	0.011 (6)
	2	4.390		0.026 (42)	4.416 (42)	
	2	4.395		0.026 (42)	4.421 (42)	
	2	4.578		0.027 (42)	4.605 (42)	
	2	4.579		0.027 (42)	4.606 (42)	
	2	4.587		0.027 (42)	4.614 (42)	
	2	4.594		0.027 (42)	4.621 (42)	
	2	4.599		0.028 (42)	4.627 (42)	
	2	4.638		0.028 (42)	4.666 (42)	
	2	4.672		0.028 (42)	4.700 (42)	
Mn-Mn	4	4.929	0.001 (5)	0.005 (25)	4.934 (25)	0.010 (2)
	2	4.937		0.005 (25)	4.942 (25)	
	2	5.012		0.005 (25)	5.017 (25)	
	2	5.030		0.005 (25)	5.035 (25)	

Table 5: EXAFS fit parameters for Li_2MnO_3 sample charged to 5 V during the 33rd cycle.

$S_0^2 = 0.7$ $\Delta E_0 = 2.0$ (7) $X_{eff} = 0.61$ (4)						
Path	N_{degen}	R_{theory} (Å)	α_{fit}	ΔR (Å)	R_{fit} (Å)	σ_{fit}^2 (Å ²)
Mn- O_{N-N}	6	1.921	-0.015 (2)	-0.029 (4)	1.892 (4)	0.0040 (6)
Mn-Mn	6	2.816	0.020 (2)	0.060 (6)	2.876 (6)	0.0099 (6)
Mn-O	6	3.409	0.003 (4)	0.010 (15)	3.419 (15)	0.005 (2)
	2	3.661		0.011 (15)	3.672 (15)	
Mn-O	12	4.422	0.005 (7)	0.022 (32)	4.444 (32)	0.008 (4)
	12	4.619		0.023 (32)	4.642 (32)	
Mn-Mn	6	4.878	0.012 (5)	0.060 (25)	4.938 (25)	0.014 (3)
	6	4.959		0.060 (25)	5.019 (25)	

Table 6: EXAFS fit parameters for Li_2MnO_3 sample discharged to 2 V during the 33rd cycle.

Path	N_{degen}	$R_{\text{theory}} (\text{\AA})$	α_{fit}	$\Delta R (\text{\AA})$	$R_{\text{fit}} (\text{\AA})$	$\sigma_{\text{fit}}^2 (\text{\AA}^2)$
$S_0^2 = 0.7$						
$\Delta E_0 = -2.4 (1.1)$						
$X_{\text{eff}} = 0.6$						
Mn- O_{N-N}	4.6 (5)	1.904	-0.004 (3)	-0.008 (6)	1.896 (6)	0.0032 (8)
Mn-Mn	2	2.845	0.010 (4)	0.029 (12)	2.874 (12)	0.0092(9)
	1	2.851		0.029 (12)	2.880 (12)	
Mn-O	2	3.513	-0.034 (4)	-0.119 (15)	3.394 (15)	0.002 (1)
	2	3.515		-0.120 (15)	3.395 (15)	
	2	3.516		-0.120 (15)	3.396 (15)	
	2	3.686		-0.125 (15)	3.516 (15)	
Mn-O	2	4.388	0.009 (5)	0.040 (24)	4.428 (24)	0.004 (2)
	2	4.390		0.040 (24)	4.430 (24)	
	2	4.395		0.040 (24)	4.435 (24)	
	2	4.578		0.041 (24)	4.619 (24)	
	2	4.579		0.041 (24)	4.620 (24)	
	2	4.587		0.041 (24)	4.628 (24)	
	2	4.594		0.041 (24)	4.635 (24)	
	2	4.599		0.041 (24)	4.640 (24)	
	2	4.638		0.042 (24)	4.680 (24)	
	2	4.672		0.042 (24)	4.714 (24)	
	2	4.693		0.042 (24)	4.735 (24)	
	2	4.721		0.043 (24)	4.763 (24)	
Mn-Mn	4	4.929	-0.005 (6)	-0.025 (30)	4.904 (30)	0.013(3)
	2	4.937		-0.025 (30)	4.912 (30)	
	2	5.012		-0.025 (30)	5.987 (30)	
	2	5.030		-0.025 (30)	5.005 (30)	

Table 7: Statistical EXAFS fit parameters for various Li_2MnO_3 samples. N_{idp} is the number of independent data points, N_{vary} is the number of fitting variables and ν is the number of degree of freedom ($\nu = N_{\text{idp}} - N_{\text{vary}}$)

Sample	$\Delta k (\text{\AA}^{-1})$	$\Delta R (\text{\AA})$	N_{idp}	N_{vary}	ν	χ^2	χ^2_{ν}	R
Pristine	3.9 - 13.5	1.0 - 5.1	24	12	12	732	59	0.008
5 V (1 st cycle)	3.8 - 11.9	1.0 - 5.0	20	12	8	2633	313	0.011
2 V (1 st cycle)	3.8 - 12.0	1.2 - 5.0	19	12	7	1615	214	0.010
5 V (33 rd cycle)	3.8 - 11.8	1.0 - 5.0	20	12	8	59	7	0.006
2 V (33 rd cycle)	3.8 - 11.8	1.0 - 5.0	20	12	8	89	11	0.013

References

- (1) Johnson, C.; Kim, J.-S.; Lefief, C.; Li, N.; Vaughey, J.; Thackeray, M. *Electrochemistry Communications* **2004**, *6*, 1085–1091.
- (2) Johnson, C.; Li, N.; Vaughey, J.; Hackney, S.; Thackeray, M. *Electrochemistry Communications* **2005**, *7*, 528–536.
- (3) Thackeray, M.; Kang, S.-H.; Johnson, C.; Vaughey, J.; Hackney, S. *Electrochemistry Communications* **2006**, *8*, 1531–1538.
- (4) Johnson, C. *Journal of Power Sources* **2007**, *165*, 559–565.
- (5) Johnson, C.; Li, N.; Lefief, C.; Thackeray, M. *Electrochemistry Communications* **2007**, *9*, 787–795.
- (6) Thackeray, M.; Kang, S.-H.; Johnson, C.; Vaughey, J.; Benedek, R.; Hackney, S. *Journal of Materials Chemistry* **2007**, *17*, 3112–3125.
- (7) Li, J.; Klöpsch, R.; Stan, M.; Nowak, S.; Kunze, M.; Winter, M.; Passerini, S. *Journal of Power Sources* **2011**, *196*, 4821–4825.
- (8) Croy, J.; Balasubramanian, M.; Kim, D.; Kang, S.-H.; Thackeray, M. *Chemistry of Materials* **2011**, *23*, 5415–5424.
- (9) Croy, J.; Kim, D.; Balasubramanian, M.; Gallagher, K.; Kang, S.-H.; Thackeray, M. *Journal of The Electrochemical Society* **2012**, *159*, A781–A790.
- (10) Boulineau, A.; Croguennec, L.; Delmas, C.; Weill, F. *Solid State Ionics* **2010**, *180*, 1652–1659.
- (11) Thackeray, M. *Progress in Solid State Chemistry* **1997**, *25*, 1–71.
- (12) Kalyani, P.; Chitra, S.; Mohan, T.; Gopukumar, S. *Journal of Power Sources* **1999**, *80*, 103–106.

- (13) Robertson, A.; Bruce, P. *Chemical Communications* **2002**, 2790–2791.
- (14) Robertson, A.; Bruce, P. *Chemistry of Materials* **2003**, *15*, 1984–1992.
- (15) Armstrong, A.; Robertson, A.; Bruce, P. *Journal of Power Sources* **2005**, *146*, 275–280.
- (16) Jain, G.; Yang, J.; Balasubramanian, M.; Xu, J. *Chemistry of Materials* **2005**, *17*, 3850–3860.
- (17) Pasero, D.; McLaren, V.; de Souza, S.; West, A. *Chemistry of Materials* **2005**, *17*, 345–348.
- (18) Yu, D.; Yanagida, K.; Kato, Y.; Nakamura, H. *Journal of The Electrochemical Society* **2009**, *156*, A417–A424.
- (19) Liu, W.; Farrington, G.; Chaput, F.; Dunn, B. *Journal of The Electrochemical Society* **1996**, *143*, 879–884.
- (20) Kelly, S.; Hesterberg, D.; Ravel, B. *Methods of Soil Analysis Part 5*; 2008; Vol. 5; pp 387–463.
- (21) Ravel, B.; Newville, M. *Journal of Synchrotron Radiation* **2005**, *12*, 537–541.
- (22) Ankudinov, A.; Ravel, B.; Rehr, J.; Conradson, S. *Physical Review B* **1998**, *58*, 7565–7576.
- (23) Calvin, S. Relationship between electron delocalization and asymmetry of the pair distribution function as determined by x-ray absorption spectroscopy. Ph.D. thesis, 2001.
- (24) Newville, M. Local thermodynamic measurements of dilute binary alloys using XAFS. Ph.D. thesis, 1995.
- (25) Ravel, B. Ferroelectric phase transitions in oxide perovskites studied by XAFS. Ph.D. thesis, 1997.
- (26) Yu, D.; Yanagida, K. *Journal of The Electrochemical Society* **2011**, *158*, A1015–A1022.
- (27) Wong, J.; Lytle, F.; Messmer, R.; Maylotte, D. *Physical Review B* **1984**, *30*, 5596–5610.

- (28) Haas, O.; Deb, A.; Cairns, E.; Wokaun, A. *Journal of The Electrochemical Society* **2005**, *152*, A191–A196.
- (29) Strobel, P.; Lambert-Andron, B. *Journal of Solid State Chemistry* **1988**, *75*, 90–98.
- (30) Rossouw, M.; Thackeray, M. *Materials Research Bulletin* **1991**, *26*, 463–473.
- (31) Rossouw, M.; Liles, D.; Thackeray, M.; David, W.; Hull, S. *Materials Research Bulletin* **1992**, *27*, 221–230.
- (32) Paik, Y.; Grey, C.; Johnson, C.; Kim, J.-S.; Thackeray, M. *Chemistry of Materials* **2002**, *14*, 5109–5115.
- (33) Sayers, D.; Stern, E.; Lytle, F. *Physical Review Letters* **1971**, *27*, 1204–1207.
- (34) Rehr, J.; Albers, R. *Reviews of Modern Physics* **2000**, *72*, 621–654.
- (35) Deb, A.; Bergmann, U.; Cairns, E.; Cramer, S. *Journal of Synchrotron Radiation* **2004**, *11*, 497–504.
- (36) Geller, S.; Cape, J.; Grant, R.; Espinosa, G. *Physics Letters A* **1967**, *24A*, 369–371.
- (37) Ouyang, C.; Shi, S.; Lei, M. *Journal of Alloys and Compounds* **2009**, *474*, 370–374.
- (38) Baur, W. *Acta Crystallographica* **1976**, *B32*, 2200–2204.
- (39) Marabello, D.; Bianchi, R.; Gervasio, G.; Cargnoni, F. *Acta Crystallographica. Section A, Foundations of Crystallography* **2004**, *A60*, 494–501.
- (40) Saint, J.; Doeff, M.; Reed, J. *Journal of Power Sources* **2007**, *172*, 189–197.
- (41) Ito, A.; Sato, Y.; Sanada, T.; Hatano, M.; Horie, H.; Ohsawa, Y. *Journal of Power Sources* **2011**, *196*, 6828–6834.
- (42) Sapre, V.; Mande, C. *Journal of Physics C: Solid State Physics* **1972**, *5*, 793–797.

- (43) Tang, W.; Kanoh, H.; Yang, X.; Ooi, K. *Chemistry of Materials* **2000**, *12*, 3271–3279.
- (44) Goodenough, J.; Kim, Y. *Chemistry of Materials* **2010**, *22*, 587–603.
- (45) Koga, H.; Croguennec, L.; Ménétrier, M.; Mannesiez, P.; Weill, F.; Delmas, C. *Journal of Power Sources* **2013**, *236*, 250–258.
- (46) Koga, H.; Croguennec, L.; Menetrier, M.; Duhil, K.; Belin, S.; Bourgeois, L.; Suard, E.; Weill, F.; Delmas, C. *Journal of the Electrochemical Society* **2013**, *160*, A786–A792.
- (47) Kanamura, K.; Toriyama, S.; Shiraishi, S.; Takehara, Z.-i. *Journal of The Electrochemical Society* **1996**, *143*, 2548–2558.
- (48) Kanamura, K. *Journal of Power Sources* **1999**, *81-82*, 123–129.
- (49) Moshkovich, M.; Cojocaru, M.; Gottlieb, H.; Aurbach, D. *Journal of Electroanalytical Chemistry* **2001**, *497*, 84–96.
- (50) Feng, Q.; Miyai, Y.; Kanoh, H.; Ooi, K. *Langmuir* **1992**, *8*, 1861–1867.
- (51) Ammundsen, B.; Aitchison, P.; Burns, G.; Jones, D.; Roziere, J. *Solid State Ionics* **1997**, *97*, 269–276.
- (52) Christensen, A.; Hansen, P.; Lehmann, M. *Journal of Solid State Chemistry* **1977**, *21*, 325–329.
- (53) Rossouw, M.; Liles, D.; Thackeray, M. *Journal of Solid State Chemistry* **1993**, *104*, 464–466.
- (54) Robertson, A.; Armstrong, A.; Bruce, P. *Chemistry of Materials* **2001**, *13*, 2380–2386.
- (55) Armstrong, A.; Paterson, A.; Robertson, A.; Bruce, P. *Chemistry of Materials* **2002**, *14*, 710–719.

Graphical TOC Entry

